Combined Method for the Modal System Identification of the Balloon-Borne Imaging Testbed

Lun Li[1]; Christopher John Damaren, Ph.D., P.Eng.[2]; Luis Javier Romualdez[3]; Calvin Barth Netterfield, Ph.D.[4]; John Wesley Hartley[5]; Mathew Notman Galloway[6]; Richard James Massey, Ph.D.[7]; and Paul Clark, C.Eng.[8]

Abstract: This paper presents a novel method for the modal system identification of a large mechanical structure by combining results from simulations and physical measurements. Specifically, reconstruction of mode shapes was accomplished by comparing simulated and measured amplitude ratios generated using a Nyquist analysis. The methodology developed in this paper improves upon traditional techniques by allowing for statistically cross-referencing relatively few sensor measurements and a relatively simple simulation model. This methodology was used to identify three major modal frequencies and mode shapes of the main aluminum honeycomb sandwich panel gondola structure of the balloon-borne imaging testbed (BIT). BIT was a stratospheric ballooning project for astronomy that was launched on September 18, 2015, from Timmins, Ontario, Canada. Ensuring that structural vibrations do not adversely affect the pointing accuracy of the on-board telescope is crucial to the success of the project. This paper also highlights some of the advantages and drawbacks of the presented methodology and suggests improvements for future applications in balloon-borne experiments. **DOI: 10.1061/(ASCE)AS.1943-5525.0000647.**

Author keywords: System identification; Modal analysis; Impulse response; Stratospheric ballooning.

Introduction

The motivation behind the development of a methodology for the modal system identification for a large structure is the balloon-borne imaging testbed (BIT). BIT was a stratospheric ballooning project for astronomy that was successfully launched on September 18, 2015, from Timmins, Ontario to an altitude of 36 km over the period of 1 night. BIT's goal was to showcase an ultra-high-accuracy pointing system that will represent a next-generation telescope for balloon-borne astronomy in the visible and near-visible (300–900 μm) spectra (CASCA 2011).

The design of the BIT gondola (Fig. 1) must allow the on-board telescope to maintain image stabilization at 50 milliarcseconds, with an integration time on the order of tens of minutes, during which the structure is subjected to external and internal forces (C. B. Netterfield, A Balloon-Borne Near-UV/Visible Light Telescope and Test-Bed, unpublished proposal, 2011). Due to the high level of pointing accuracy required, the normally imperceptible oscillations created by stepper motors, ball bearings, and frame resonances can prove detrimental to the resulting image quality (Rhodes et al. 2012; Barthol et al. 2011).

The analyses introduced in this paper are integral in the design of the on-board control system in order to achieve the desired pointing requirement. Although not a direct focus of this paper, a potential application of its results is the incorporation of the identified mode shapes and frequencies in the augmentation of a control system.

Scientific Motivations

The scientific importance of this paper is three old. Firstly, prior to BIT, analyses dedicated to understanding specifically the modal behaviors of the structure was seldom and minimally performed for balloon-borne gondolas (Rhodes et al. 2012; Pascale et al. 2008; Soler et al. 2014; Barthol et al. 2011), if at all, and are often considered ex post facto (e.g., Barthol et al. 2011; Pascale et al. 2008).

Secondly, the mathematical technique that the authors introduced in this paper, the comparison of amplitude ratios, is not used in past analyses of structural dynamics. This technique has the clear advantage of not needing a piece of specialized equipment—an impact hammer with a force transducer—which can not only be expensive but also introduce new sources of error to the system. Much like how balloon-borne telescopes are a much cheaper alternative to space telescopes with minimum sacrifices in atmospheric obscuration, this method of modal system identification with amplitude

[1]Engineer Researcher, Dept. of Physics, Univ. of Toronto, 60 St. George St., Toronto, Canada M5S 1A7; Graduate Student, Institute for Aerospace Studies, Univ. of Toronto, 4925 Dufferin St., Toronto, Canada M3H 5T6 (corresponding author). E-mail: lun.li@mail.utoronto.ca

[2]Professor, Institute for Aerospace Studies, Univ. of Toronto, 4925 Dufferin St., Toronto, Canada M3H 5T6.

[3]Graduate Student, Institute for Aerospace Studies, Univ. of Toronto, 4925 Dufferin St., Toronto, Canada M3H 5T6.

[4]Professor, Dept. of Physics, Univ. of Toronto, 60 St. George St., Toronto, Canada M5S 1A7; Professor, Dept. of Astronomy and Astrophysics, Univ. of Toronto, 50 St. George St., Toronto, Canada M5S 1A7.

[5]Graduate Student, Dept. of Physics, Univ. of Toronto, 60 St. George St., Toronto, Canada M5S 1A7.

[6]Graduate Student, Dept. of Physics, Univ. of Toronto, 60 St. George St., Toronto, Canada M5S 1A7.

[7]Royal Society University Research Fellow, Centre for Advanced Instrumentation, Durham Univ., South Rd., Durham DH1 3LE, U.K.

[8]Head of Engineering, Centre for Advanced Instrumentation, Durham Univ., South Rd., Durham DH1 3LE, U.K.

Note. This manuscript was submitted on December 21, 2015; approved on April 6, 2016; published online on June 22, 2016. Discussion period open until November 22, 2016; separate discussions must be submitted for individual papers. This paper is part of the ***Journal of Aerospace Engineering***, © ASCE, ISSN 0893-1321.

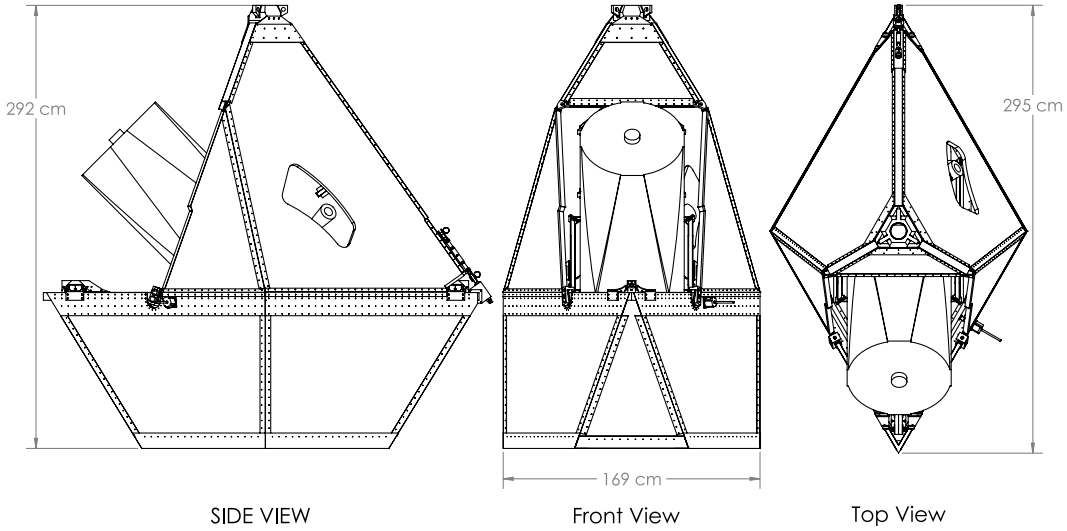

Fig. 1. BIT gondola is approximately 3 m tall from the base to the pivot joint and weighs around 800 kg, and it is constructed primarily out of aluminum honeycomb panels; this gondola was designed by the author between the summers of 2012 and 2013; its construction was achieved by everyone at the University of Toronto High Bay who is on the BIT team between 2013 and 2015; the gondola is comprised of three independently rotating gimbals, the largest and most ostensible of which, the outer frame, is the subject of the analyses performed in this paper

ratios is a much cheaper alternative to the classic technique of using force transducers.

Thirdly, the Balloon-Borne Imaging Testbed was the prototype mission for a new class of ultra-high-precision balloon-borne pointing systems. This means that balloons are now a viable medium for future high-precision astronomical telescopes and will become ubiquitous due to their advantages over terrestrial telescopes. Therefore, this motivates a quick and reliable method to perform system identification of the BIT gondola and can be deemed as *necessary* for future balloon-borne experiments.

Approach and Methodology

Simply stated, this study intends to determine the characteristic frequencies and mode shapes of the BIT gondola within a range of frequencies that are of concern. There are two general ways which this problem can be solved: through finite-element analysis (FEA) simulation and through direct measurements. Each approach on its own has many methods and implementations all with varying benefits and shortcomings.

FEA Simulation

This category of modal system identification techniques has the obvious benefits of versatility: the retrieval of results does not require the physical system, the mode shapes can be easily represented visually, and the information regarding the entire gondola can be retrieved to arbitrary precision. However, it is often infeasible to completely rely on FEA for system identification due to several fundamental drawbacks inherent to simulation. Namely, all of the benefits stated in the preceding sentence rely on an accurate FEA model of the physical system, and this is often difficult to achieve due to computational limitations; the greater the accuracy of the model, the greater the computational time. A simplified model requires many assumptions that, if chosen improperly, may misrepresent the system.

Physical Measurements

This category of modal system identification techniques has the advantage of accuracy as the behavior of the system is being directly measured by sensors. However, these sensors are also highly constraining because they are physical objects. If every sensor measures a single point on the gondola, information regarding mode shapes is only known at those measured locations. It can get increasingly difficult to add more sensors to represent the continuum that is the physical gondola.

Combining Systems

Due to their advantages and limitations, the two systems are combined in the system identification of the BIT gondola. Specifically, the procedure can be stated as follows:

1. Create an FEA model of the BIT gondola;
2. Simulate the FEA model to retrieve characteristic frequencies and mode shapes;
3. Determine locations of greatest amplitude for modes that fall within the frequency range of interest;
4. Place sensors (accelerometers) onto the BIT gondola at the locations of interest;
5. Collect impulse response data from the sensors (in the time domain);
6. Process the data and create Fast Fourier Transform (FFT) results;
7. Identify peaks to determine natural frequencies and amplitude ratios;
8. Identify spread to determine the damping ratios;
9. Use FFT circle plots (Nyquist plots) to identify phases between sensors;
10. Match measured mode shapes with the simulated mode shapes; and
11. Interpret the results.

The corroboration between the simulation results and the physical measurements implies that the true (more accurate) frequencies will be represented by the physically measured results and the true (more complete) mode shape will be represented by the simulation

result. This combination gives a better constrained system by utilizing the more accurate frequency measurement from the accelerometers while utilizing mode shape information from the FEA. Each of the preceding steps is described in detail in the following sections.

Mechanical Description

The mechanical component of BIT can be summarized as a mechanism that accommodates the pointing degrees of freedom, maintains the pointing accuracy, and withstands the various forces imposed on a balloon-borne telescope. Three gimbal frames are used to allow telescope rotation in the three independent axes: the inner frame, middle frame, and outer frame. In order to minimize low-frequency vibrations of the structure, a material that has a great strength to weight ratio, aluminum honeycomb sandwich panels, was chosen as the main structural element for all three frames (L. Li, A Design Study of The Balloon-Borne Imaging Testbed, unpublished report, 2013).

Constructing the Simulation Model

For the simulation analysis of BIT, the simulation model was derived from the full mechanical model of the gondola, which was modeled in the computer-aided design software SolidWorks. The simulation analysis was completed using its simulation package *SolidWorks Simulation*. Since a direct simulation of the entire structure with all its intricacies would prove overly complicated, the geometry of the structure must be greatly simplified in order to practically perform the simulations. This was done by approximating the entire structure as a shell, which provides two main benefits: (1) the complexity of the simulation is significantly reduced (compared to a solid body simulation); and (2) unrealistic edge effects due to corner connections that are generally found in solid body simulations are removed.

One important simplification made was that the modeling only included the major structural component, the outer frame. This is done because the outer frame is assumed to be sufficiently decoupled from the other frames due to the minimally constrained contact points between them.

From the documentation on the frequency analysis in *SolidWorks Simulation*, it is known that the solution of its frequency analysis is determined by solving the eigenvalue problem

$$(\mathbf{K}_{ee} - \omega_\alpha^2 \mathbf{M}_{ee})\mathbf{q}_\alpha = \mathbf{0}, \alpha = 1,2,3, \ldots$$

where $\mathbf{K}_{ee}$ and $\mathbf{M}_{ee}$ = respectively, the stiffness and mass matrices of the system; ω_α = natural frequencies; and $\mathbf{q}_\alpha$ = eigenvectors (mode shapes) (*SolidWorks API*). Therefore, it is crucial to accurately input the stiffness and mass of the gondola model.

Creating the Correct Shell

The modeling of the aluminum honeycomb sandwich panels was done manually by defining a shell that has an equivalent bending stiffness *EI* as the panels supplied by the vendor Teklam, Corona, California. Through-thickness and in-plane effects, such as core shear, are not considered because they are considered to be small compared to plate bending. It can be shown that the *EI* of a sandwich panel is approximately the product of the area moment *I* and the Young's modulus *E* of the surface sheets (Hexcel 2000). Thus, a shell thickness of 12.4 mm, which would represent the same *I* as two 0.5 mm (0.02 in.) sheets kept at 24.9 mm (0.98 in.) apart, was used for the shell definition.

Table 1. Properties of the Custom Shell Material Defined in SolidWorks Simulation

Property	Value	Unit	Reference material
Elastic modulus in *X*	69,000	$N \cdot mm^2$	AL3003-h18
Poisson's ratio in *XY*	0.33	—	AL3003-h18
Shear modulus in *XY*	25,000	$N \cdot mm^2$	AL3003-h18
Mass density	523	$kg \cdot m^3$	Computed
Tensile strength in *X*	200	$N \cdot mm^2$	AL3003-h18
Yield strength in *XY*	185	$N \cdot mm^2$	AL3003-h18
Shell thickness	12.4	mm	Computed

Note: properties are taken/computed from the facesheet material (AL3003-H18 aluminum alloy) of the Teklam AA207-33-1000 panels (Teklam 2005).

In addition, the density of the material was recalculated so that a 12.4-mm-thick sheet would have the same mass per area as the Teklam sheet. A custom material was defined in the frequency analysis. The final property assignments are documented in Table 1.

Defining Distributed Masses

In order to create a high-accuracy mass matrix in the eigenequation, distributed masses were assigned to the shell in addition to its own mass (Fig. 2). Geometric regions where the batteries are located were partitioned in the model to represent the batteries. A mass of 18 kg (40 lb) was assigned to each of the areas, representing the weight of the individual batteries. A separate rigid shell plate was created for the reaction wheel, whose diameter is approximately the same as that of the real reaction wheel (100 cm), sitting on a rigid cylinder, whose height is approximately the same as that of the reaction wheel (20 cm). A separate partition ring was defined on the plate at which a distributed mass of 45 kg (100 lb) was assigned. Extra masses were added to all edge joints where they were estimated using the weight of the joining aluminum sheets, fasteners (bolts, nuts, and washers), and epoxy glue. Significant electronics boxes were also added by defining new partitions.

The self-mass of the shell structure is assigned automatically when the density of the material is defined as in Table 1. In certain areas, an extra shell layer was added in the model to represent extra reinforcement material. Specifically, this was done to the sheet that joins the midplane ring to the lower half of the outer frame. This is a rather convenient method of reinforcing material without redundantly defining a new type of sheet. However, this was not done to the bottommost sheet of the outer frame, where there are two layers of the 25.4 mm (1 in.) aluminum honeycomb sheets. For this bottom panel, a new equivalent shell was defined for a double-layered honeycomb panel.

Simulation

Once a represented shell model is created, the next step is to simulate the system using *SolidWorks Simulation*. One of the most crucial aspects of this simulation process is to properly define the boundary conditions for the structure. *SolidWorks Simulation* allows for the definition of a variety of simulation conditions such as fixed, sliding, pinned, and free. Unfortunately, it does not provide a direct definition for a gondola hanging from a tether, which is the real system. However, it is known that a tether does not fix the motion of the gondola at any position. Therefore, the closest boundary condition definition would be to define the structure as a free body, without any constraints.

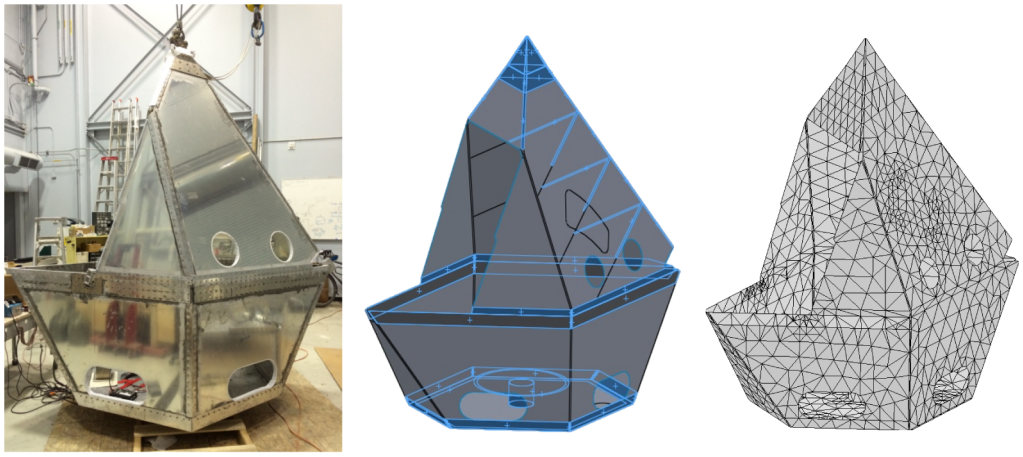

Fig. 2. (a) Physical gondola of BIT used as the subject of this paper; (b) simulation shell created based on the gondola; specially assigned mass distributions are highlighted and marked with a plus sign (+); (c) mesh used in the simulation

Identification of Sensor Placement Locations

Given the undamped linear system solved by *SolidWorks Simulation*, the physical interpretation of a mode is when each point in the structure vibrates at the same frequency and reaches maximum deflections simultaneously. Therefore, it would be advantageous to place the sensors at the spatial antinodes (or locations of greatest structural deflection) to maximize the signal to noise ratio for the sensors (Bai et al. 2008).

Fig. 3 shows the simulated mode shapes of the first six elastic modes of BIT's outer frame. Based on the observed structural deformations, sensor locations are heuristically chosen in attempt to maximize the measured amplitudes. The final choices are shown in Fig. 4.

Sensor Selection, Installation, and Readout

The physical portion of the system identification process was accomplished using accelerometers, which are commonly used in modal identification techniques (Baqersad et al. 2014; Avitabile et al. 2006; Bai et al. 2008). There are several advantages to this particular choice of sensors. Firstly, accelerometers are inexpensive and can be easily acquired. The miniaturization of microelectromechanical systems (MEMS) have made these inertial sensors the size of a pinhead and they can be fastened anywhere in the form of a breakout board. Secondly, the directions of the accelerometer measurements are the same as those of the mode shapes. As the second derivative of a sine function is another sine function, the acceleration of the modal vibrations maintains the shape of the modal vibration with a constant scaling. Thirdly, accelerometers can preserve much more information at higher frequencies. In the Fourier domain, the amplitude is proportional to frequency squared, so the peaks in the higher frequencies would appear much more prominently. Because of these reasons, a total of 21 analog accelerometer channels were used in the physical data collection in the system identification process.

The data were collected asynchronously at an average rate of approximately 1,260 Hz, which is much greater than the control limit of the gondola, specifically the telescope optics piezoelectric actuator that operates at approximately 50 Hz. For each trial, several tens of seconds of time-streams were collected in order to be able to capture finer details in the frequency domain. However, all trials were limited to be under 5 min as higher-frequency noise would dominate for longer trials with diminishing gain in the resolution of lower frequency responses. These time-stream data were then processed using *MATLAB*.

Impulse Response

An easy (both mathematically and practically) and common way to excite a system across all frequencies is by applying an impulsive input (Baqersad et al. 2014; Eggers and Stubbs 1994; Ewins 1995). Mathematically, a perfect impulse [a Dirac-delta function $\delta(t)$] corresponds to a constant value across all frequencies in the Fourier domain (Ewins 1995). This simplicity will be shown to be algebraically advantageous in the derivations. Practically, an impulse can be approximated simply by an impact from a hammer. To prevent damage to the gondola, a rubber mallet was chosen for this task.

Ideally, the response from an impulse does not depend significantly on where the impulse is applied. This greatly reduces potential complexity of the experiment by reducing it from a multiple-input multiple-output (MIMO) system to a single-input multiple-output (SIMO) system (Baqersad et al. 2014). This fact was corroborated by performing impulse response measurements at multiple impact locations.

Structural Model

The mathematical description of the system begins with the partial differential equation describing the deformation field $\mathbf{w}(\mathbf{r}, t)$ of the elastic structure, where $\mathbf{w}$ is a function of spatial location $\mathbf{r}$ and time t under an impulsive excitation at location $\mathbf{r}_a$ with a strength f in the direction $\mathbf{n}_a$

$$\mathcal{M}\ddot{\mathbf{w}}(\mathbf{r}, t) + \mathcal{D}\dot{\mathbf{w}}(\mathbf{r}, t) + \mathcal{K}\mathbf{w}(\mathbf{r}, t) = \mathbf{n}_a\delta(\mathbf{r} - \mathbf{r}_a)f\delta(t) \quad (1)$$

where $\mathcal{M}$, $\mathcal{D}$, and $\mathcal{K}$ = mass, damping, and stiffness operators, respectively (Maia and Silva 2001).

The undamped eigenvalue problem (as solved in *SolidWorks Simulation*) is

$$-\omega_\alpha^2\mathcal{M}\psi_\alpha + \mathcal{K}\psi_\alpha = \mathbf{0}, \alpha = 1,2,3, \cdots \quad (2)$$

where ψ_α and ω_α = αth mode shape (eigenfunction) and undamped natural frequency (root of the eigenvalue), respectively.

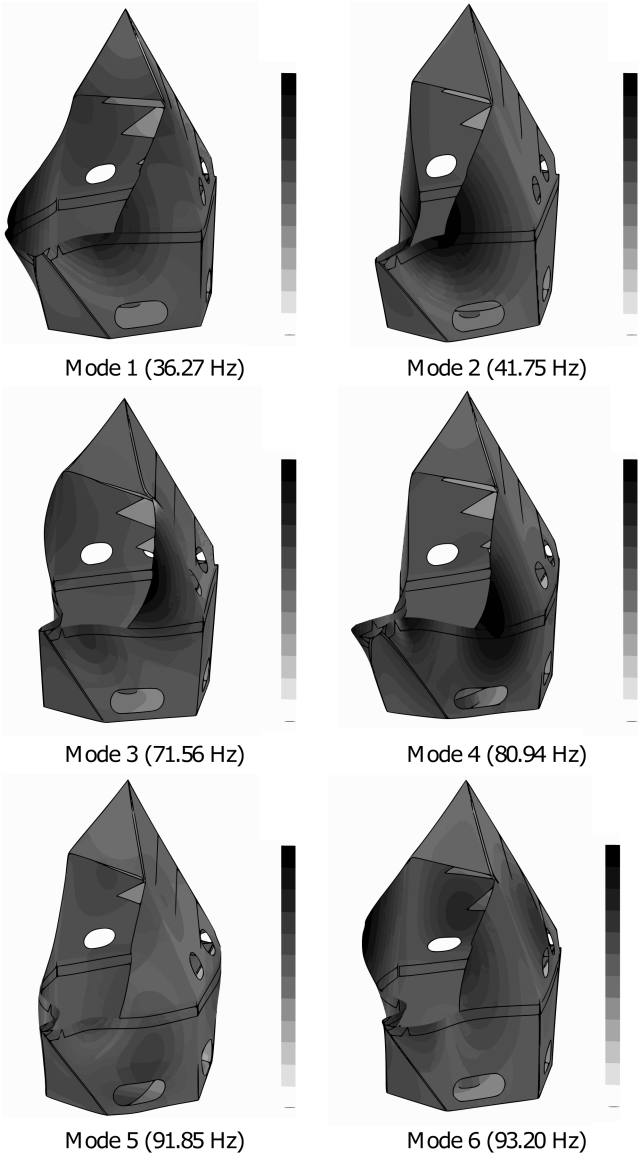

Fig. 3. First six elastic body modes (following the six rigid body modes of three rotations and three translations) as solved by *SolidWorks Simulation*; the actual magnitudes of the displacement results are unimportant as they are normalization dependent, while the relative magnitudes (amplitude ratios) are not

As such, $\mathbf{w}$ can be written as a modal decomposition in the form of

$$\mathbf{w}(\mathbf{r},t)=\sum_{\alpha=1}^{\infty}\psi_\alpha(\mathbf{r})\eta_\alpha(t) \tag{3}$$

where η_α = modal coefficients.

The eigenfunctions possess the following orthogonality properties:

$$\int_V \psi_\alpha^T \mathcal{M}\psi_\beta dV=\delta_{\alpha\beta} \tag{4}$$

$$\int_V \psi_\alpha^T \mathcal{K}\psi_\beta dV=\omega_\alpha^2\delta_{\alpha\beta} \tag{5}$$

where $\delta_{\alpha\beta}$ = Kronecker delta. In addition, if it is assumed that damping in the system is relatively small and the modes are

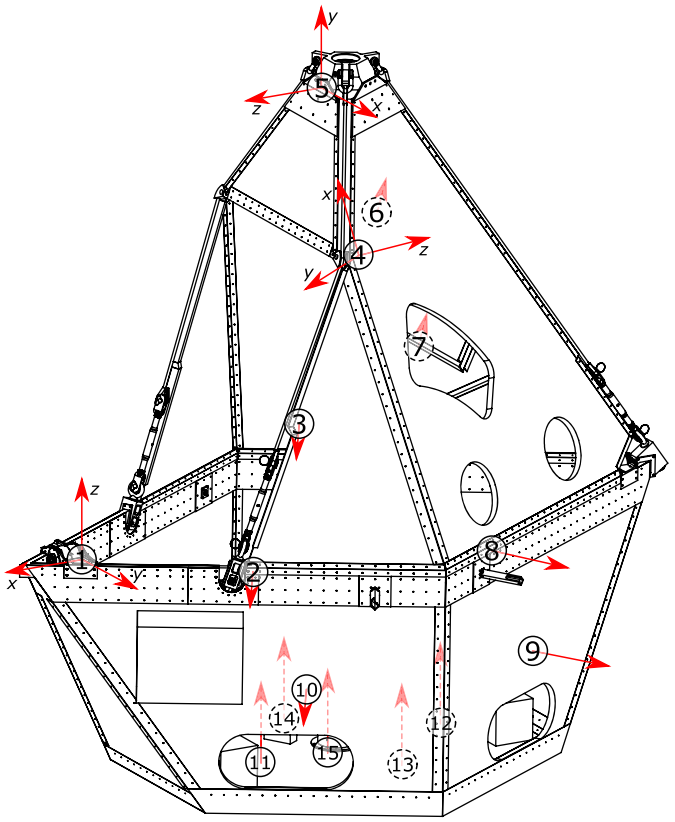

Fig. 4. Physical layout of the accelerometer placements; Sensors 1, 4, and 5 are triaxial accelerometers and the rest are single-axis accelerometers (where the deformations are transverse to the sheet surfaces); dashed markers represent sensors not in view

orthogonal to the damping operator, the following approximation can be made:

$$\int_V \psi_\alpha^T \mathcal{D}\psi_\beta dV=2\zeta_\alpha\omega_\alpha\delta_{\alpha\beta} \tag{6}$$

where ζ_α = αth damping ratio (Maia and Silva 2001).

Using modal decomposition as well as the orthogonality conditions described in Eqs. (5) and (6), substituting Eq. (3) into Eq. (1) allows it to be diagonalized and simplified to

$$\ddot{\eta}_\alpha(t)+2\zeta_\alpha\omega_\alpha\dot{\eta}_\alpha(t)+\omega_\alpha^2\eta_\alpha(t)=\psi_{a,\alpha}f\delta(t),\alpha=1,2,3,\ldots \tag{7}$$

where $\psi_{a,\alpha}=\boldsymbol{\psi}_\alpha^{\mathrm{T}}(\mathbf{r}_a)\mathbf{n}_a$ = constant representing the mode shape evaluated at the impulse location in the direction of the impulse.

Taking the Laplace transform of Eq. (7) and solving for η_α gives

$$\eta_\alpha(s)=\frac{\psi_{a,\alpha}f}{s^2+2\zeta_\alpha\omega_\alpha s+\omega_\alpha^2} \tag{8}$$

where s = Laplace transform variable and notation is abused by letting $\eta_\alpha(s)$ be the Laplace transform of $\eta_\alpha(t)$.

Sensor Model

Letting $\mathbf{r}_s$ and $\mathbf{n}_s$ be the location and the measurement direction of an accelerometer, the output measurement, y can be expressed as

$$y(t)=\mathbf{n}_s^T\ddot{\mathbf{w}}(\mathbf{r}_s,t) \tag{9a}$$

$$= \sum_{\alpha=1}^{\infty} \psi_{s,\alpha} \ddot{\eta}_\alpha(t) \tag{9b}$$

where $\psi_{s,\alpha} = \mathbf{n}_s^T \boldsymbol{\psi}_\alpha(\mathbf{r}_s)$ = constant representing the amplitude of the mode shape evaluated at the accelerometer location in the direction of the accelerometer axis. Taking the Laplace transform of Eq. (9*b*) and substituting Eq. (8) gives

$$y(s) = \sum_{\alpha=1}^{\infty} \psi_{s,\alpha} \eta_\alpha(s) s^2 \tag{10a}$$

$$= \sum_{\alpha=1}^{\infty} \frac{C_\alpha s^2}{s^2 + 2\zeta_\alpha \omega_\alpha s + \omega_\alpha^2} \tag{10b}$$

$$= \sum_{\alpha=1}^{\infty} C_\alpha H_\alpha(s) \tag{10c}$$

where $C_\alpha = \psi_{s,\alpha} \psi_{a,\alpha} f$ = constant value representing a relative amplitude, and

$$H_\alpha(s) = \frac{s^2}{s^2 + 2\zeta_\alpha \omega_\alpha s + \omega_\alpha^2} \tag{11}$$

Eq. (10*b*) fully describes sensor measurements as a function of modal parameters in the Laplace domain.

Peak Identification

Once the data from the accelerometer measurements from the impulse response were acquired, all computations are carried out using *MATLAB*. These steps include resampling the time series, finding the time of impulse, converting time domain data to frequency domain using the Fast Fourier Transform (FFT), and creating frequency and amplitude plots. Plotting the amplitude versus frequency of the FFT results in a log-log plot and yields a fairly recognizable shape for damped elastic structures, shown in Fig. 5. The frequencies of the resonant modes can be easily identified by measuring the frequencies corresponding to the peaks in this plot.

Circle Plots

Another method of plotting FFT data is by directly plotting the complex values on a imaginary versus real plot (Ewins 1995; Maia and Silva 2001). These circle plots (or Nyquist plots) contain a great deal of unique information that cannot be represented by amplitude plots. Starting with the description of the sensor model in the Laplace domain, Eq. (10*b*) can be converted using Eq. (11) into the Fourier domain by substituting $s = j\omega$, where $j = \sqrt{-1}$: $y_\alpha(j\omega) = C_\alpha H_\alpha(j\omega)$, yielding

$$y_\alpha(j\omega) = \frac{-C_\alpha \omega^2 (-\omega^2 + \omega_\alpha^2 - 2\zeta_\alpha \omega_\alpha j\omega)}{(-\omega^2 + \omega_\alpha^2 + 2\zeta_\alpha \omega_\alpha j\omega)(-\omega^2 + \omega_\alpha^2 - 2\zeta_\alpha \omega_\alpha j\omega)} \tag{12a}$$

$$= \frac{-C_\alpha \omega^2 [(-\omega^2 + \omega_\alpha^2) - 2\zeta_\alpha \omega_\alpha j\omega]}{(-\omega^2 + \omega_\alpha^2)^2 + 4\zeta_\alpha^2 \omega_\alpha^2 \omega^2} \tag{12b}$$

which when plotted, looks like a lopsided circle that is almost symmetrical about the imaginary axis and almost tangent to the real axis (Fig. 6).

Substituting $\omega = \omega_\alpha$ produces

$$y_\alpha(j\omega_\alpha) = \frac{jC_\alpha \omega_\alpha^4 2\zeta_\alpha}{4\zeta_\alpha^2 \omega_\alpha^4} = j\frac{C_\alpha}{2\zeta_\alpha} \tag{13}$$

which means that $y_\alpha(j\omega)$ evaluated at the natural frequency ω_α lies on the imaginary axis.

In general, the damped natural frequency can be expressed as

$$\omega_{d\alpha} = \sqrt{1 - \zeta_\alpha^2}\,\omega_\alpha \tag{14a}$$

$$= \left[1 - \frac{1}{2}\zeta_\alpha^2 + O(\zeta_\alpha^4)\right]\omega_\alpha \tag{14b}$$

where ζ_α = damping ratio. Therefore, $\omega_{d\alpha} \doteq \omega_\alpha$ to the order of ζ_α.

Now it is time to solve for the frequency that results in an amplitude of $-3dB$, which is a factor of $1/\sqrt{2}$. Starting from $|y_\alpha(j\omega_{3\text{ dB}})| = C_\alpha/(2\sqrt{2}\zeta_\alpha)$, by expanding, rearranging, simplifying, and approximating using the Taylor expansions, at the following is obtained:

$$\omega_{3\text{ dB}} \doteq \begin{cases} \omega_\alpha(1 - \zeta_\alpha) & = \omega_1 \\ \omega_\alpha(1 + \zeta_\alpha) & = \omega_2 \end{cases} \tag{15}$$

where ω_1 = frequency smaller than ω_α at which the amplitude is 3 dB (or $\sqrt{2}$ times) lower than the peak amplitude; similarly, ω_2 = frequency greater than ω_α at which the amplitude is 3 dB (or $\sqrt{2}$ times) lower than the peak amplitude.

Rearranging the expressions for ω_1 and ω_2, then ζ_α can be solved for with

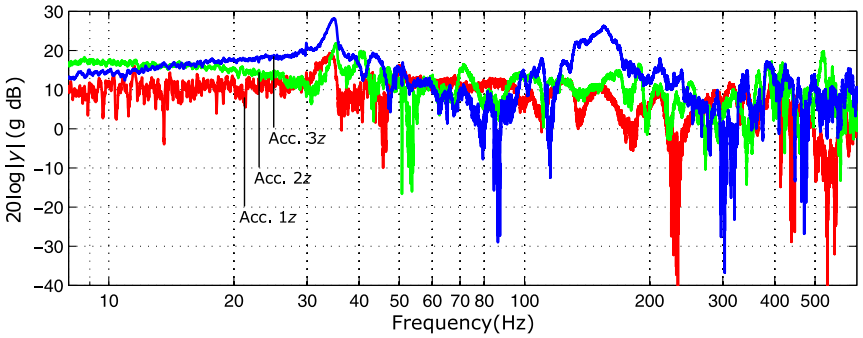

Fig. 5. Examples of the amplitude versus frequency data of the accelerometer measurements of Locations 1, 2, and 3 (given in Fig. 4) smoothed using a 10-sample moving average; an obvious mode can be observed around 34.5 Hz as peaks are observed in all three sensors

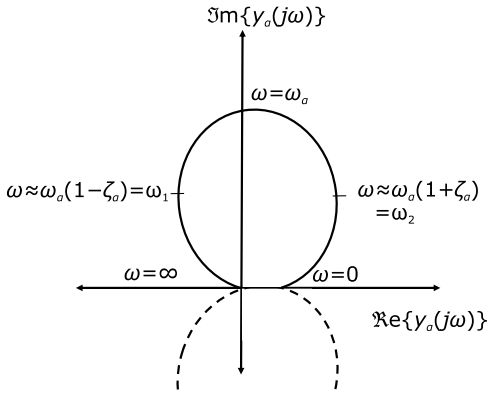

Fig. 6. Theoretical circle plot of accelerometer measurements plotted in the Laplace domain; the dotted curve represents the complex conjugate set mirrored about the real axis; ω_1 and ω_2 correspond to the 9 o'clock and 3 o'clock positions of the circle, respectively

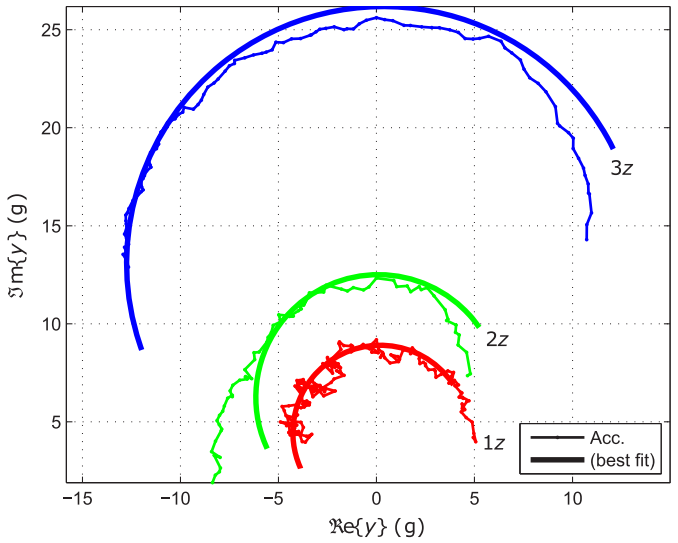

Fig. 7. Samples of measured circle plots near the 34.5 Hz peak (ω_1 to ω_2 range) fitted using a least-squares circular regression

Table 2. Damping Ratios of the Fundamental (34.5 Hz) Mode Calculated Using the 3 dB Approximation at Three Sensor Locations

Sensor (z)	ω_1 (Hz)	ω_2 (Hz)	ω_α (Hz)	ζ_α (%)
1	32.02	35.04	34.17	4.4
2	34.33	35.49	35.19	1.6
3	33.50	35.37	34.77	2.7

$$\zeta_\alpha = \frac{\omega_2 - \omega_1}{2\omega_\alpha} \tag{16}$$

which represents the viscous damping ratio in Eq. (6). An example of the calculations for ζ_α is presented in Table 2.

Least-Squares Fit for Nyquist Plot

In order to find the best C_α that fits the experimental data, a least-squares fit can be performed that solves for C_α that minimizes the cost function $\mathfrak{J} = \sum_i |Y_\alpha(j\omega_i) - C_\alpha H_\alpha(j\omega_i)|^2$ where i is the index along the FFT result's vector (Maia and Silva 2001). Recall that H_α is defined in Eq. (11). In order to minimize $\mathfrak{J}$, take the derivative with respect to C_α and set it to zero

$$\frac{d\mathfrak{J}}{dC_\alpha} = -2\sum_i \Re e[Y_\alpha^*(j\omega_i)H_\alpha(j\omega_i)] + 2C_\alpha \sum_i |H_\alpha(j\omega_i)|^2 = 0 \tag{17}$$

Solving for C_α yields

$$C_\alpha = \frac{\sum_i \Re e[Y_\alpha^*(j\omega_i)H_\alpha(j\omega_i)]}{\sum_i |H_\alpha(j\omega_i)|^2} \tag{18}$$

The physical interpretation of this least-squares method is shown in Fig. 7, where the best-fit lines represent $C_\alpha H_\alpha$ and the measured curves represent y_α.

Another method of solving for C_α is by using the geometrical fact that the circle plot of accelerometer measurements is approximately a circle with the maximum sitting on the imaginary axis (Fig. 6). Combining with Eq. (16), C_α can be directly expressed as $C_\alpha = 2\zeta_\alpha \Im m[y_\alpha(j\omega_\alpha)]$.

The comparison between the two methods is presented in Table 3, which reveals that the differences are small. Therefore, only the maximum amplitudes will be used to compute the amplitude ratios.

Table 3. Comparing C_α Solved Using the Least-Squares Method and the Maximum-Amplitude Method at Three Sensor Locations

Sensor (z)	Least squares	Maximum amplitude	Difference (%)
1	0.7832	0.8084	3.2
2	0.4002	0.3946	1.4
3	1.4137	1.3833	2.2

Note: The label z indicates the z-direction of the triaxial accelerometers.

Amplitude Ratios

Recall in Eq. (10*b*), the combined amplitude coefficient $C_\alpha = \psi_{s,\alpha}\psi_{a,\alpha}f$ for accelerometer measurements. Even though C_α can be computed from the circle plots of the physical measurements, no knowledge is had regarding the terms inside of C_α, namely, the sensor measurement amplitude coefficient $\psi_{s,\alpha}$, the plant amplitude coefficient $\psi_{a,\alpha}$, and the impact strength f.

In the simulation model, the modal amplitudes are normalized for each mode shape and do not actually represent physical amplitudes of the gondola. Therefore, the comparison between C_α with simulation measurements must be done with ratios where the unknown constant coefficients ($\psi_{a,\alpha}$ and f) are cancelled out, leaving only the ratios of the sensor measurements

$$\frac{C_\alpha(\mathbf{r}_1)}{C_\alpha(\mathbf{r}_2)} = \frac{\psi_{s,\alpha}(\mathbf{r}_1)}{\psi_{s,\alpha}(\mathbf{r}_2)} \tag{19}$$

where $\mathbf{r}_1$ and $\mathbf{r}_2$ = two different sensor locations.

It is crucial to recognize that the true benefit of using this ratio is that it does not depend on the strength of the impact (f) or where the impact takes place ($\psi_{a,\alpha}$). In fact, this would be true for other types of responses as well: the Fourier transform of the input cancels in the ratio. However, the impulse response (or near-impulse response) has the added advantage of having a constant (or near-constant), specifically non-zero, amplitude across all frequencies. Its cancellation in the amplitude ratios would not only maintain

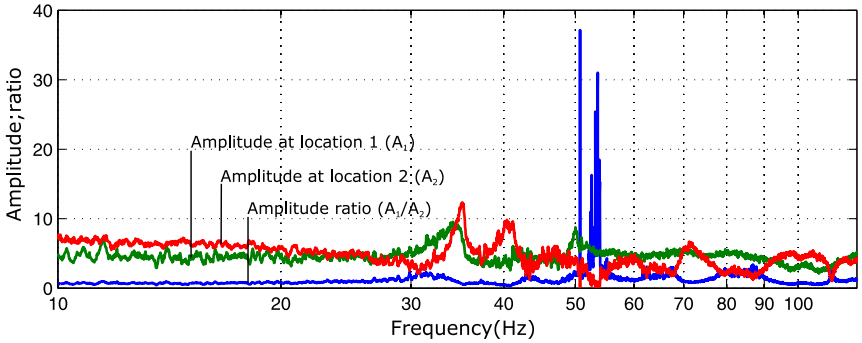

Fig. 8. Visualization of a set of amplitude ratios computed from two sets of measured amplitudes; the amplitudes at Location 1 is divided by the amplitudes of Location 2 across all frequencies

a near-constant signal to noise ratio but also avoid division-by-zero situations that may be true for other responses. Additionally, the constant (or near-constant) amplitude across all frequencies is also required for the Nyquist (circle fit) analysis in order to produce the desired circles. However, it was shown previously that the C_α's resulted from the least-squared fit of the Nyquist circles were very close to those resulted from just measuring the peaks, which does not require a flat response. In principle, one could determine the shape of the impulse from the FFT of a single accelerometer measurement using the mathematical form of the response in the vicinity of several modes.

Matching Mode Shapes with Natural Frequencies

Now that all of the mathematics behind the modeling of the BIT structure have been established, the ultimate and most crucial portion of the procedure can now be discussed: the actual identification of the mode shapes of the gondola. Due to the large sets of imperfect data collected through the numerous sensors and repeated impacts and the inability to fully manipulate the simulation model, certain heuristics are developed for this identification procedure. The procedure can be broken down into five steps:

1. Extracting modal amplitudes from simulation at the sensor locations;
2. Determining largest amplitude for each simulated mode shape;
3. Calculating the amplitude ratios for all sensors of each mode by dividing by the largest amplitude of that mode;
4. Take amplitude ratios of measured data of accelerometer impulse response; and
5. Compare measured amplitude ratios with simulated amplitude ratios.

Steps 1 to 3 are fairly straightforward. However, there are a couple of immediate problems trying to perform Steps 4 and 5: the measured results are continuous spectra, meaning there are no distinct modes to select the ratios. Additionally, the measured results have much of the noise of the real structure expressed in them as well as noise from the measurements.

The latter problem can be ameliorated by lightly smoothing the amplitude versus frequency curves using a simple averaging filter. From the raw data, there are approximately 1,260 indices per Hertz (in the frequency domain). By taking the average of a sliding window of 10 samples in the frequency domain, the amplitude plots will be much smoother (to a resolution of approximately 0.008 Hz) and less likely to produce erroneous spikes in the ratios.

To solve the former problem, a ratio is taken for every frequency step. To do this, the FFT results of all 21 sensors are converted to amplitudes at the 15 locations. Specifically, triaxial sensors at Locations 1, 4, and 5 (Fig. 4) are converted using $\sqrt{|\mathbf{x}|^2+|\mathbf{y}|^2+|\mathbf{z}|^2}$ where $\mathbf{x}$, $\mathbf{y}$, and $\mathbf{z}$ are complex values (from the FFT results), and the rest of the amplitudes extracted by taking $|\mathbf{z}|$ of the FFT results from the single-direction sensor measurements.

Once all of the amplitudes are extracted, they are divided by the amplitudes of the chosen sensor for each frequency to act as the denominator, in this case, the amplitudes of Sensor 2. An example of this process can be seen in Fig. 8. This is done for all of the amplitudes of the FFT results for all of the impacts to produce the ratios.

In Step 4, 15 amplitude ratios are generated for each frequency step and for every impact experiment. In Step 5, the goal is to determine which of these matches best for each of the 15 amplitude ratios for each of the simulated modes (Step 3).

Comparison Metric

There are many ways to evaluate how well the measured ratios match the simulated ratios. In the literature, χ^2 tests and covariance analyses are some common methods to identify correlations between sets of data. Without invoking metaparameters that are necessary to correctly perform and interpret those methods, the authors decided to use the simple yet intuitive method of comparing the sum of squared differences (called norm^2), between the simulated 15 amplitudes and the measured 15 amplitudes for every frequency and impact.

A squared difference, rather than a signed difference, was chosen because the simulated amplitude measurements that were made were unsigned. With signed amplitude ratio measurements, a signed difference sum, such as $\pm$norm^2 or $\pm$norm, would be a better metric. Additionally, since the items being compared are ratios, they are dimensionless and are invariant to scaling.

Since a smaller value corresponds to a better match, in order to highlight values that are close to each other, an inverse of the squared difference sum value ($1/\text{norm}^2$) is taken to generate the ordinate-axis of the figure. Figs. 9 and 10 show the results of such a comparison for the second and third simulated mode shapes. At this point, the comparison portion of the experiment can be concluded.

Results and Applications

The results of the comparisons between simulated and measured amplitude ratios are summarized in Fig. 11. Three mode shapes are confidently identified at 34.5, 40.9, and 79.2 Hz.

The goal of this experiment is to discover a methodology to determine the natural frequencies and mode shapes of a large

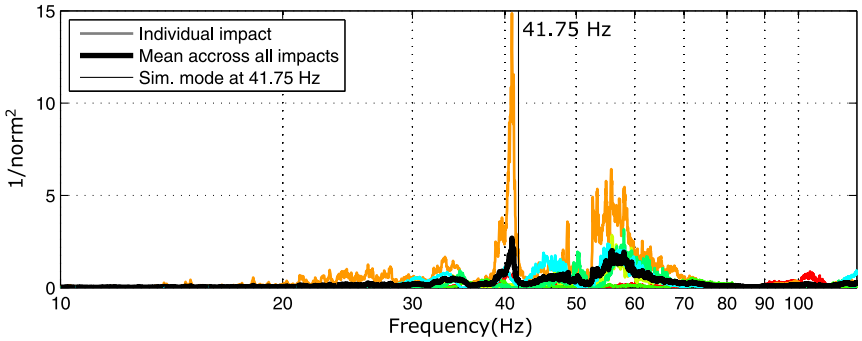

Fig. 9. Inverse of the sum of the squared differences between the measured and simulated ratios of elastic Mode 2 (at the simulated natural frequency of 41.8 Hz); the measured and simulated ratios seem to be highly correlated for this particular mode

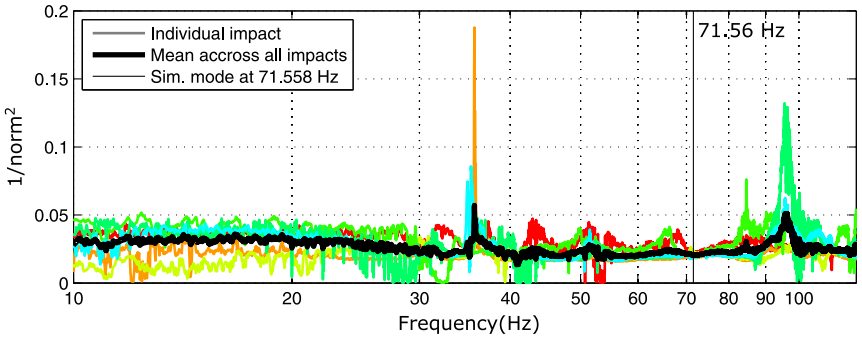

Fig. 10. Inverse of the sum of the squared differences between the measured and simulated ratios of elastic Mode 3 (at the simulated natural frequency of 71.6 Hz); no correlation is observed at the modal frequency; although a peak can be seen around 35 Hz, the scale is much less than that of Fig. 9, indicating that the peaks in this figure are likely from noise

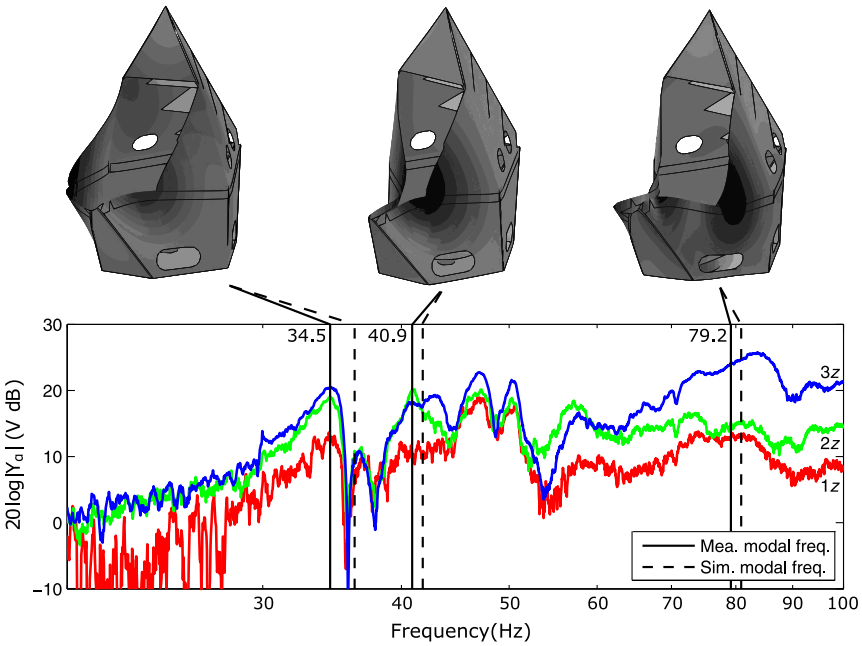

Fig. 11. Matching of mode shapes and frequencies, showing both simulated and measured natural frequencies, as well as a selection of the FFT amplitude plots of the input response measurements; three mode shapes are identified at 34.5, 40.9, and 79.2 Hz

mechanical structure. This was completed through the system identification of the BIT gondola. This methodology can be used in the development of future balloon-borne experiments where it is important to determine structural vibrations for high-fidelity control systems. Originally, the control system of BIT was to incorporate the identified frequencies and mode shapes. However, it was decided that this was not necessary for the successful operation of BIT, as the lowest mode (34.5 Hz) is above the control bandwidth (30 Hz maximum).

Even through the mode shapes were unused in the final control system of BIT project, the natural frequencies determined in this experiment might still be important for the control system of BIT. Due to the sensitive nature of the pointing controls, band-pass (boxcar) filters were used on the gyro input during BIT's flight to mitigate resonances at around 25–30 Hz.

Discussion

There are many interesting observations that can be made about the comparison between simulated and measured amplitude ratios. It is immediately obvious that there are frequencies with greater than average correlations. Specifically, there are discernible peaks at around 34.5, 40.9, 47.7, 58.3, and 79.2 Hz. An example of such a peak is shown in Fig. 9 for the 40.9 Hz mode. The vertical line in Fig. 9 shows the natural frequency of the corresponding mode as simulated by *SolidWorks Simulation*. On the other hand, no obvious correlation can be observed in several simulated modes, such as Mode 3, Mode 5, and Mode 6. It seems like with the exception of these, the natural frequencies all correspond to an observable peak. An example of this is shown in Fig. 10, where the ratios are taken to match Mode 3 of the simulated modes.

Mean Correlation Data for Natural Frequencies

The most obvious thing to be said about the mean correlation data (black bold curves in Figs. 9 and 10) is that its peaks correspond to natural frequencies. Specifically, there is a simulated frequency that matches the peaks of 34.5, 40.9, and 79.2 Hz. By extension, the mode shapes corresponding to the natural frequencies represent those of the gondola expressed at those frequencies.

Although this interpretation is simple and direct, there are several discrepancies that potentially undermine the correctness and usefulness of the results. For instance, there is a peak at around 58.3 Hz that does not match any of the simulated natural frequencies; there is more than one peak per mode shape; and, the averages over all the impacts are significantly different from the results of the individual impacts.

Error Characterization and Areas for Improvement

For a large experiment such as this, involving a significant amount of engineering heuristics, there exist many areas for improvement. Several of these areas are presented here that might facilitate potential future experiments.

Multiple Peaks in the Least-Squares Plots

In the least squares fit of the Nyquist circles [Eq. (18)], the goal was to match the simulated modal amplitude ratios with the measured modal amplitude ratios. This was done by taking the sum of the squared difference between the two for each frequency. Ideally, if the modal amplitude ratios match perfectly (or very closely) for that mode, the sum of the squared difference would be near zero. Since all of the mode shapes are different, that would also mean the sum of the least-squares difference would not be near zero for all other frequencies. If it were a perfect setup, a single peak would be expected in each of Figs. 9 and 10, representing the natural frequency corresponding to the mode shape. Instead, many peaks can be seen, even worse for the individual (unaveraged) impacts.

The explanation for this phenomenon is actually quite simple: the mode shapes are not entirely independent. For instance, the first two elastic modes have similar relative modal amplitudes at the same sensor locations. Modes 3 and 4 have similar shapes but out of phase about the symmetrical plane. Between Modes 2, 3, and 4, the bellowing motions of the L-corners at the front of the gondola are all observed. Between the modes chosen for analyses, the differences between them are observably fewer than the similarities between them. This is what causes the average (black bold) curves in Figs. 9 and 10 to look similar to each other.

A possible way to overcome this problem is that rather than comparing all of the ratios together, individual ratios must be selected out to characterize the differences and similarities between every two mode shapes. Great care would be needed to avoid confirmation bias when selecting measurements for comparison. The downside to this method is that the process can no longer be automated, at least it will not be as simple as finding the least-squares difference.

Unsigned Ratios

In addition to the similar mode shapes, this problem is exacerbated by the fact that the amplitude ratios are generated using only the amplitudes of the peaks, rather than using the least-squares circle fits. This would also mean that the ratios are unsigned; it would be impossible to tell if geometries are moving in-phase or out-of-phase with each other. Consequently, this problem can be ameliorated by using the C_α ratios solved by taking the least-squares fit and comparing them to the signed amplitude ratios measured from a signed measurement of the simulated amplitudes. The latter was not done due to the difficulty in extracting the directional amplitudes from *SolidWorks Simulation*. Even though the usage of only the norm of the amplitudes is sufficient in this work as a proof-of-concept, the authors expect much clearer results can be achieved using directional amplitudes that are extracted from a more user-accessible simulation package.

Impact Locations

Even though that, theoretically, the measurement results should be independent from the impact location, observations show that the results vary quite significantly depending on the location of impact. As can be clearly seen in Figs. 9 and 10, different impacts resulted in vastly different matches with amplitude ratios even though general trends are maintained.

Although the discrepancy is undesirable, there exists a simple explanation for this phenomenon. Take for instance the difference between an impact that was performed at the bow of the gondola and an impact that was performed at the stern of the gondola. The bow impact resulted in highly correlated data whereas the stern impact resulted in much flatter data. This is because the bow of the gondola is where the modal amplitude is maximum for most of the simulated modes whereas the stern of the gondola is where the modal amplitude is the least for most of the modes. This would mean that the structural response for bow impact would be much greater than that of the stern impact, as by the time the shock propagated to the front to excite the bow modes, it would have been significantly damped.

Damping

Many of the imperfections of the results are caused by working with a highly damped structure. Using the fact that $C_\alpha = 2\zeta_\alpha \Im\mathrm{m}\{y_\alpha(j\omega_\alpha)\}$, ζ_α can be approximated using the formula

$(\omega_2 - \omega_1)/(2\omega_\alpha)$, where ω_1 and ω_2 are the frequencies surrounding the natural frequency that correspond to approximately 3 dB below the peak amplitude. As presented Table 2, all of the damping ratios seem to be below 10%, which is consistent with what is expected of honeycomb structures such as the BIT gondola.

The calculations in Table 2 are done for some of the most prominent peaks in the results. For the less-prominent (more spread-out) peaks, the damping ratios would be much higher. The greater the damping ratio, the greater the difference between real and theoretical results. Most of the discrepancies in the modal frequencies can be attributed to this fact.

Mass Consistency

A crucial consistency check for the integrity of the model definition is that the total mass should be fairly close to the mass of the real structure. This step is critical in the accuracy of the simulation results, because, in a naïve sense, the natural frequencies are proportional to the mass of a structure. Unfortunately, this was not done for the simulation model of the outer frame because of the limited access the user has on the simulation data of *SolidWorks Simulation*. It is likely that this has contributed to a portion of the inaccuracies in the results.

A trick that can be employed to reverse engineer the simulation mass is by recognizing the fact that the normalization of the resultant mode shapes is generally done through the mass matrix (which was checked by simulating a trivial case). For an unconstrained body, the modal analysis would result in six rigid-body modes, –generally three in translation and three in rotation. If at least one translation mode is sufficiently decoupled from the other five rigid-body modes, its magnitude can be used to calculate the total mass of the system. Using the orthogonality property of Eq. (4), $\int_V \boldsymbol{\psi}_\alpha^{\mathrm{T}} \mathscr{M} \boldsymbol{\psi}_\beta \mathrm{d}V = \delta_{\alpha\beta}$, for any of the three translation modes of the system, the mode shape would be independent of the mass operator

$$\boldsymbol{\psi}_\tau^T \left[\int_V \sigma \mathbf{1} dV \right] \boldsymbol{\psi}_\tau = 1 \tag{20}$$

$$\boldsymbol{\psi}_\tau^T \boldsymbol{\psi}_\tau \int_V \sigma dV = 1 \tag{21}$$

$$\boldsymbol{\psi}_\tau^T \boldsymbol{\psi}_\tau m = 1 \tag{22}$$

$$m = \frac{1}{\boldsymbol{\psi}_\tau^T \boldsymbol{\psi}_\tau} \tag{23}$$

where $\boldsymbol{\psi}_\tau$ = any rigid body translation mode; σ = local density (or the elemental mass in the case of the FEA) of the system; $\mathbf{1} = 3 \times 3$ identity matrix; and m = total mass of the body. Using Eq. (23), the total mass of the system is simply the inverse-square of the modal amplitude of any translation mode.

This simple formula offers a nice sanity check for the mass of the system if a translation mode can be identified from the results. For the simulations performed in this paper, the model is estimated using this method to be around 250 kg, which is consistent with the mass of the gondola. An iterative process would be required to match the simulated mass and the physical mass. Even though this process was not considered for this paper, it is highly recommended for future experiments.

Single Shell Simulation

To avoid overly complicating the problem, the simulation was performed on the shell model for the outer frame only, even though the measurements were done on the gondola with all three frames. This simplification slightly undermines the accuracy of the results. However, since there is minimum coupling between the frames, they can be treated as independent systems. A future iteration might include an accurate modeling of all three frames of the gondola for simulation. This can be done by defining flexible connections between the frames using pin connections. This pin connection allows for a rotational degree of freedom but is constrained in all other directions. It is of great interest to see the effects of coupling between the frames on the simulation results.

Summary and Conclusion

A method of combining simulation results with measurement results for the purposes of modal system identification was developed in this paper. For the BIT gondola's outer frame honeycomb sandwich panel structure, the three modes were confidently identified at 34.5, 40.9, and 79.2 Hz. Their corresponding mode shapes were also identified to be the breathing motions of the gondola front opening. These mode shapes were generated using *SolidWorks Simulation* and were compared with measured values through amplitude ratios. The frequencies were generated from the peaks in the amplitude versus frequency curves derived from the physical measurements, which were made using analog accelerometers placed throughout the gondola. This method of comparing amplitude ratios introduces a novel way of identifying mode shapes without the necessity of a prohibitively large number of sensors or an impractical amount of detail in the simulation model, because the information between the simulation and physical measurements are cross referenced statistically.

The identified mode shapes can be valuable because they can provide insights on the structural changes that can be performed to improve the resonant behavior of the system. Additionally, a much more sophisticated project design might be able to incorporate the frequency and mode shape results in a highly advanced control algorithm that can take advantage of the otherwise deleterious elastic behaviors. Future iterations of the identification techniques may involve (1) the analyses of the measurement results in greater detail, such as the incorporation of phase and directional measurements; (2) creating a better and more computationally accessible simulation model, possibly using another more-dedicated simulation package; and (3) refining the measurement systematics for greater accuracies of measurement results.

Notation

The following symbols are used in this paper:

C_α = $\psi_{s,\alpha}\psi_{a,\alpha}f$ (relative amplitude constant);
$\mathcal{D}$ = damping operator;
E = Young's modulus;
EI = bending stiffness (product of E and I);
f = impulse strength coefficient;
H_α = Nyquist circle of the αth mode;
I = second moment of area;
i = FFT output vector index;
$\mathfrak{J}$ = least squares cost function;
$\Im\mathrm{m}$ = imaginary component of input complex function;
j = $\sqrt{-1}$ (imaginary unit);
$\mathcal{K}$ = partial differential stiffness operator;
$\mathbf{K}_{ee}$ = stiffness matrix of an elastic body;
$\mathscr{M}$ = partial differential mass operator;
$\mathbf{M}_{ee}$ = mass matrix of an elastic body;
m = total mass of an elastic body;
$\mathbf{n}_a$ = impulse direction vector;

$\mathbf{n}_s$ = sensor measurement direction vector;
O = big O notation;
$\mathbf{q}_\alpha$ = eigenvector (mode shape) of an elastic body;
$\Re$e = real component of input complex function;
$\mathbf{r}$ = spatial location vector;
$\mathbf{r}_a$ = impulse location vector;
$\mathbf{r}_s$ = sensor measurement location vector;
s = Laplace domain complex variable (frequency);
t = time;
V = space occupied by the elastic body;
$\mathbf{w}$ = vector function of the deformation field of an elastic body;
X = axial direction of the material definition in SolidWorks Simulation;
XY = shear direction of the material definition in SolidWorks Simulation;
$\mathbf{x}$ = FFT result vector of the x-component measurements of a triaxial accelerometer;
$\mathbf{y}$ = FFT result vector of the y-component measurements of a triaxial accelerometer;
y = sensor measurement output ($y(t)$ in time domain; $y(s)$ in frequency domain);
y_α = $C_\alpha H_\alpha$ [the component of $y(s)$ corresponding to the αth mode];
$\mathbf{z}$ = FFT result vector of the z-component measurements of a triaxial accelerometer;
α = modal index;
β = modal index;
δ = Dirac delta function;
$\delta_{\alpha\beta}$ = 1 if $\alpha = \beta$; 0 if $\alpha \neq \beta$ (Kronecker delta);
ζ_α = damping ratio of the αth mode;
η_α = modal coordinate of the αth mode;
σ = mass density (elemental mass);
τ = translational rigid body modal index;
$\psi_{a,\alpha}$ = $\boldsymbol{\psi}_\alpha^T(\mathbf{r}_a)\mathbf{n}_a$ (amplitude of mode shape evaluated at impulse location);
$\psi_{s,\alpha}$ = $\mathbf{n}_s^{\mathrm{T}}\boldsymbol{\psi}_\alpha(\mathbf{r}_s)$ (amplitude of mode shape evaluated at accelerometer location);
$\boldsymbol{\psi}_\alpha$ = eigenfunction (mode shape) of the αth mode;
ω = Fourier domain variable (frequency);
ω_1 = frequency less than ω_α at which the amplitude is 3 dB below the peak;
ω_2 = frequency greater than ω_α at which the amplitude is 3 dB below the peak;
ω_α = natural frequency of the αth mode;
$\omega_{d\alpha}$ = damped natural frequency of the αth mode;
$(\cdot)^{\mathrm{T}}$ = vector transpose;
$\dot{(\cdot)}$ = first-order differentiation with respect to time t;
$\ddot{(\cdot)}$ = second-order differentiation with respect to time t; and
$(\cdot)^*$ = complex conjugate operator;
$\mathbf{0}$ = null vector; and
$\mathbf{1}$ = identity matrix.

References

Avitabile, P., Singhal, R., Peeters, B., and Leuridan, J. (2006). "Modal parameter estimation for large, complicated MIMO tests." *Sound Vib.*, 40(1), 14.

Bai, Z., Zhao, Y., Ma, W., and Tian, H. (2008). "Modal analysis for small satellite system with finite element method." *2nd Int. Symp. on Systems and Control in Aerospace and Astronautics, 2008, ISSCAA 2008*, IEEE, Piscataway, NJ, 1–5.

Baqersad, J., Poozesh, P., Niezrecki, C., and Avitabile, P. (2014). *Comparison of modal parameters extracted using MIMO, SIMO, and impact hammer tests on a three-bladed wind turbine*, Springer, Bethel, CT, 185–197.

Barthol, P., et al. (2011). "The sunrise mission." *Solar Phys.*, 268(1), 1–34.

CASCA (Canadian Astronomical Society). (2011). "Report of the long range plan 2010 panel." ⟨http://www.casca.ca/lrp2010/11093_AstronomyLRP_V16web.pdf⟩ (May, 2013).

Eggers, D. W., and Stubbs, N. (1994). "Structural assessment using modal analysis techniques." *Proc., 12th Int. Modal Analysis, Society of Photo-Optical Instrumentation Engineers (SPIE) Conf. Series*, Society for Experimental Mechanics, Bethel, CT.

Ewins, D. J. (1995). *Modal testing: Theory and practice*, 2nd Ed., Vol. 6, Research Studies Press, Letchworth, Hertfordshire, England.

Hexcel. (2000). "Hexweb honeycomb sandwich design technology." *Rep. No. AGU 075b*, Cambridge, U.K.

Maia, N. M. M., and Silva, J. M. M. (2001). "Modal analysis identification techniques." *Philos. Trans.: Math. Phys. Eng. Sci.*, 359(1778), 29–40.

MATLAB version R2012b. [Computer software]. MathWorks, Natick, MA.

Pascale, E., et al. (2008). "The balloon-borne large aperture submillimeter telescope: Blast." *Astrophys. J.*, 681(1), 400–414.

Rhodes, J., et al. (2012). "Space-quality data from balloon-borne telescopes: The high altitude lensing observatory (HALO)." *Astropart. Phys.*, 38, 31–40.

Soler, J. D., et al. (2014). "Design and construction of a carbon fiber gondola for the spider balloon-borne telescope." *Proc., SPIE*, SPIE, Washington, DC, 91450T-1–91450T-16.

SolidWorks API [Computer software]. Dassault Systèmes SolidWorks, Waltham, MA.

Teklam. (2005). "AA207-33-1000 product datasheet." ⟨http://beaerospace.com/wp-content/uploads/sites/6/2014/12/AA207-33-1000.pdf⟩ (Jun. 2013).